FEAfix: FEA Refinement of Design Equations for Synchronous Reluctance Machines

FEAfix: FEA Refinement of Design Equations for Synchronous Reluctance Machines / Ferrari, Simone; Pellegrino, Gianmario. - In: IEEE TRANSACTIONS ON INDUSTRY APPLICATIONS. - ISSN 0093-9994. - STAMPA. - 56:1(2020), pp. 256-266. [10.1109/TIA.2019.2954797]

FEAfix: FEA Refinement of Design Equations for Synchronous Reluctance Machines

Simone Ferrari, *Student Member, IEEE* and Gianmario Pellegrino, *Senior Member, IEEE*
Department of Energy "*Galileo Ferraris*"
Politecnico di Torino, Turin, Italy
Email: simone.ferrari@polito.it, gianmario.pellegrino@polito.it

***Abstract*—The Synchronous Reluctance (SyR) machine is an attractive substitute of induction motors and synchronous PM motors thanks to its high efficiency and low cost of manufacturing. Yet, its design cannot be considered a mature topic, especially for what concerns the rotor geometry. Design equations were proposed for SyR machines by different authors, representing a good starting point and a useful guideline for designers, but they are far from giving accurate results. Conversely, the design procedures based on finite element analysis tend to rely on the brute force of optimization algorithms rather than on the designer's insight. In this work, a comprehensive design procedure is proposed, where design equations are complemented by the use of the iron saturation curve and the new fast FEA approach named FEAfix. This corrects the equations results via few static FEA simulations per design plane, i.e. per family of machines, rather then by FEA simulating the single machine under design. The general conclusion is drawn that the considered analytical model alone tend to overestimate torque by as much as 40% (average on the design plane). Upon augmenting equations with the saturation curve, the average overestimate drops in the vicinity of 10% error. Finally, the proposed FEAfix refinement guarantees 2% to 1% torque evaluation error, depending on the admitted computational time. High precision is therefore obtained while retaining the generality of the analytical approach.**

I. INTRODUCTION

Synchronous Reluctance (SyR) machines were proposed in the last years as a cost competitive and efficient alternative to other kind of machines in many fields of application [1] - [3]. Compared to Permanent Magnet Synchronous Machines (PMSM), the SyR solution reduces the cost of manufacturing, thanks to the absence of rare-earth Permanent Magnets (PM). These advantages are balanced by a lower torque per volume, a parameter-dependent control strategy and a less standardized design procedure. Against Induction Machines (IMs), the SyR machines exhibits higher efficiency, due to the absence of rotor cage loss [1], and manufacturing simplification. On the other hand, IMs have in general a better power factor and well established design procedures.

The literature reports different approaches to the design of SyR machines. Most of them use Finite Element Analysis (FEA) and optimization algorithms massively. The referenced examples relying to some extent to analytical approaches are [4] - [8]. In [5] the effect of iron saturation is neglected. In [4] and [6] iron saturation is evaluated iteratively using a magnetic model circuit with high number or nodes to accurately predict the shape of the airgap flux density. In [7] the analytical model is used at machine sizing level and then FEA validated. Also [8] uses the analytical approach to define the main rotor quantities, and then relies on FEA for performance estimation and optimization.

All other popular design approaches include FEA and optimization algorithms, as in [9] - [12]. The final precision is much higher in these latter cases, but very often at the expense of high computational time and little to no insight of the designer on the results.

This paper proposes a novel equation-based design approach, where progressive improvements of the initial linear model are presented and tested. Iron saturation is included via interpolation of the relative B-H curve. Secondly, the FEA is used to fix the residual error of the analytical design equations. The proposed procedure relies on simulating a few relevant machines to correct the torque and power factor estimation of a large family of designs. In this way, the generality and computational speed of the analytical model are preserved, together with the precision of the FEA approach.

This paper extends the work presented in [13] with new contributions. These include the better mathematical formulation of the saturation factor k_{sat}, the sensitivity analysis towards variations of thermal loading, iron flux density and iron ribs flux density, and the torque and power factor sensitivity analysis towards misestimate of the different inductances involved in the model. Another new contribution is the chart reporting computational time versus model accuracy, for step-by-step comparison of the improvements proposed in the paper respect to the full FEA approach.

All the procedures and the equations presented in the paper are embedded in the form of Matlab script into the open-source platform SyR-e [14], based on the FEA client FEMM [15].

II. DESIGN EQUATIONS

The dq flux linkages of the SyR machine can be written as:

$$\begin{cases} \lambda_d = L_d\, i_d = (L_{md} + L_\sigma)\, i_d \\ \lambda_q = L_q\, i_q = (L_{mq} + L_\sigma)\, i_q \end{cases} \tag{1}$$

where i_d and i_q are the dq current components, and L_d, L_q are the respective inductances, equal to the sum of the magnetizing terms L_{md} and L_{mq} (distinct for each axis) and the leakage term L_σ (same for both axis). All the inductances depend on geometric inputs and number of turns.

The thermal loading factor k_j is the design input that determines the current loading. It is defined as the allowed copper loss by the stator outer surface, according to:

$$k_j = \frac{\frac{3}{2}\, R_s\, i_0^2}{2\pi R L} \tag{2}$$

where i_0 is the nominal current (peak), R_s is the stator resistance, R is that stator outer radius and L the stack length. Typical values of k_j (verified on several prototypes and commercial motors) are $k_j = 1.5 \sim 3\, kW/m^2$ for non-ventilated machines, $k_j = 5 \sim 12\, kW/m^2$ for machines with forced ventilation and $k_j = 12 \sim 20\, kW/m^2$ for water-cooled machines. The rated current i_0 relates to thermal loading according to:

$$N_s i_0 = \sqrt{k_j \cdot \frac{k_{Cu}}{\rho} \cdot \frac{L}{L + l_{end}} \cdot \frac{\pi\, R\, A_{slots}(x, b)}{9}} \tag{3}$$

where N_s the number of turns in series per phase, k_{Cu} is the slot filling factor, ρ is the copper resistivity, l_{end} is the end-winding length and A_{slots} is the total cross-section of the slots (sum of all slots) that varies both with the parameters x and b, defined later.

The fixed design inputs are the stator outer radius R and length L, the pole-pair p and slot/pole/phase q numbers, and the peak flux density B_{Fe}. Key input data are reported in Table I.

A. Torque expression

Assuming p pole pairs, torque is computed as:

$$T = \frac{3}{2}\, p\, (\lambda_d\, i_q - \lambda_q\, i_d) \tag{4}$$

Substituting (1) in (4) it results in:

$$T = \frac{3}{2}\, p\, (L_{md} - L_{mq})\, i_0^2 \cdot \frac{sin\,(2\,\gamma)}{2} \tag{5}$$

Where $i_d = i_0\, cos(\gamma)$, $i_q = i_0\, sin(\gamma)$ and γ is the argument of the current vector with respect to the d axis, as shown in Fig. 1. Equation 5 highlights an important property: the leakage inductance does not affect the output torque.

B. Power factor expression

The power factor $cos\varphi$ is the second key performance figure of the SyR machine, besides torque. Neglecting the stator resistance voltage drop, the power factor is evaluated as:

$$cos\varphi = sin(\gamma - \delta) \tag{6}$$

where γ and δ are the current and flux linkage angles respectively, both evaluated starting from the d-axis (see Fig.1). Further manipulation leads to expressing the power factor as a function of the inductances and current phase angle γ, as done for torque [16]:

$$cos\varphi = \sin\gamma \cdot \left(1 - \frac{L_q}{L_d}\right) \cdot \sqrt{\frac{1}{1 + (\frac{L_q}{L_d} \cdot \tan\gamma)^2}} \tag{7}$$

Notice that, imposed the current amplitude, the power factor is function of L_d, L_q and γ. Different from torque (5), $\cos\varphi$ (7) is also function on the leakage inductance L_σ.

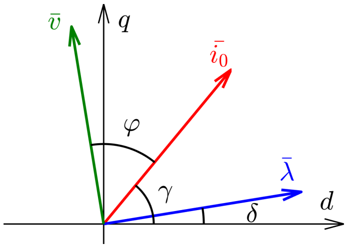

Fig. 1. Current and flux linkages names and conventions in the dq plane

C. Per-unit design factors x and b

Following the approach initiated in [17] and [18], the rotor/stator split ratio x (8) and the airgap/iron flux density ratio b (9) are defined as the key design inputs:

$$x = \frac{r}{R} \tag{8}$$

$$b = \frac{B_g}{B_{Fe}} \tag{9}$$

These will be used to explore the expected design outputs over the bi-dimensional design domain x, b. The terms r and R in (8) are the rotor and stator outer radii, respectively (see Fig. 2-3). In (9), B_{Fe} is the peak flux density in the stator yoke and B_g is the peak flux density in the airgap. All geometric quantities will be expressed in terms of x and b, to define torque and power factor as functions of (x, b). This will lead to the design plane $T(x, b)$, $cos\varphi\,(x, b)$, used for easy visualization of the performance trends versus the geometric inputs, with negligible computational effort.

D. d-axis and iron core design

The d axis is the maximum permeance direction of the machine, i.e. the main flux direction. Therefore, the iron core is designed according to the d-axis equations, for both the stator and the rotor.

Under the assumption of sinusoidal (i.e. fundamental) airgap flux density distribution of amplitude B_g, the d-axis airgap flux under one pole is:

$$\Phi_d = 2\, r\, L\, B_g \tag{10}$$

Upon substitution of (8) and (9), the design factors x and b are put in evidence:

$$\Phi_d = 2\, R\, L\, B_{Fe} \cdot x\, b \tag{11}$$

Imposing the yoke flux equal to half the pole flux, the yoke length l_y results:

$$l_y = \frac{R}{p} \cdot x\, b \tag{12}$$

This is valid having neglected the presence of slot leakage flux. The tooth width is evaluated considering the flux in a tooth equal to the airgap flux across one slot pitch $\frac{2\,\pi\, r\, L}{6\, p\, q}$ at peak flux density B_g, given the peak tooth flux density $\frac{B_{Fe}}{k_t}$:

$$w_t = \frac{2\pi r}{6pq}\, k_t\, \frac{B_g}{B_{Fe}} = \frac{2\pi R}{6pq} \cdot k_t\, \cdot x\, b \tag{13}$$

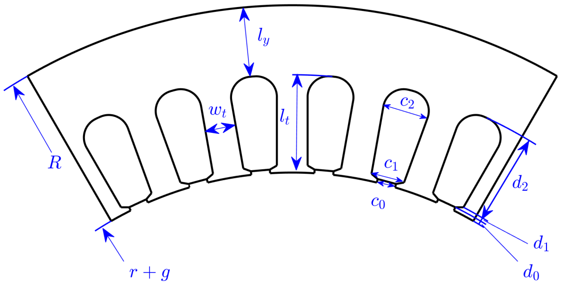

Fig. 2. Nomenclature of the stator dimensions.

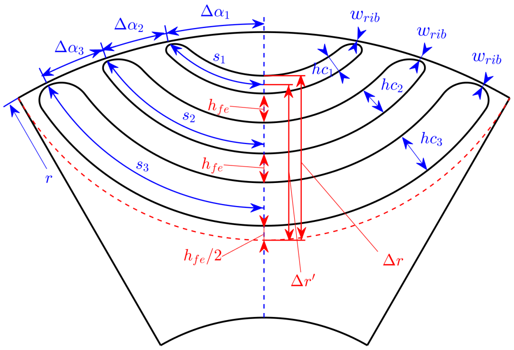

Fig. 3. Nomenclature of the rotor dimensions.

The tooth factor is commonly $k_t < 1$, so to saturate teeth more than the back iron [19].

Dealing with the rotor flux carriers design, we consider that they must carry the airgap flux of half pole, same as said for the stator back iron. The widths of the considered flux carriers are indicated in Fig.3 in red: please note that the segment on top of the pole is not considered as a proper flux carrier and neglected in the following. A design constraint is set to guarantee that the total size of the rotor carriers equals the yoke size l_y: this implies that also the peak flux density in the rotor equals the one in the stator yoke, B_{Fe}. The design of flux barriers and carriers widths will be completed in the next subsection.

Assuming ideal iron (infinite permeability), the magnetizing inductance L_{md} is inversely proportional to the airgap length g, given the winding factor k_w and the Carter's factor k_c [19].

$$L_{md} = \frac{6}{\pi}\,\mu_0 \left(\frac{k_w\, N_s}{p}\right)^2 \frac{R\,L}{k_c\, g} \cdot x \tag{14}$$

The $d-$axis Magneto-Motive Force (MMF) needed to impose the airgap flux density value $B_g = b\,B_{Fe}$ follows from the Ampere's law, still with ideal iron:

$$\frac{3}{\pi}\,\frac{k_w\, N_s}{p}\, i_d = \frac{k_c\, g \cdot B_{Fe}}{\mu_0} \cdot b \tag{15}$$

Otherwise expressed, such MMF determines the excitation current i_d corresponding to the design inputs B_{Fe} and b, assuming that N_s is known:

$$i_d = \frac{\pi}{3}\,\frac{k_c\, g}{\mu_0}\,\frac{p}{k_w\, N_s}\, B_{Fe} \cdot b \tag{16}$$

The d current is a portion of the thermal current i_0.

E. q-axis and rotor barriers design

The q axis is the maximum reluctance direction of the machine. The design of q-axis related quantities aims at minimizing the flux flowing in this direction, through minimization of the L_{mq}/L_{md} ratio by design of the rotor flux barriers. The inductance L_{mq} consists of two main terms named the circulating L_{cq} and flow-through L_{fq} inductances [17], [18]. The former accounts for the stator flux paths crossing the airgap locally, without crossing the air barriers, while the latter term accounts for the flux paths crossing the rotor barriers from pole to pole.

The circulating inductance component, in per-unit of L_{md}, is obtained by integrating the difference between the sinusoidal stator MMF and the averaged staircase MMF, indicated in Fig. 4 [18].

$$\frac{L_{cq}}{L_{md}} = 1 - \frac{4}{\pi} \sum_{k=1}^{n_{lay}} f_k^2\, \Delta\alpha_k \tag{17}$$

n_{lay} is the number of flux barriers, $\Delta\alpha_k$ is the k^{th} flux barrier position along the airgap, as defined in Fig. 3 and f_k is the corresponding component of $q-$axis MMF, according to Fig. 4. The sinusoidal curve in blue is the fundamental component of the stator MMF along the q axis.

The per unit inductance (17) is influenced by the flux barrier number n_{lay} and their positions at the airgap $\Delta\alpha_k$, $k = 1, 2, ...n_{lay}$. Please notice that the barriers widths hc_k have no influence here. The angular positions are selected according to a regular pitch, following the golden rules for torque ripple minimization formulated in [20]. In the reported example, the stator has 12 slots per pole pair and all considered rotors will have the pitch of 16 equivalent slots (12 + 4, according to [20]). This translates into $\Delta\alpha_2 = \Delta\alpha_3 = \frac{2\pi}{p\,16}$ and $\Delta\alpha_1 = 1.5\,\Delta\alpha_2$ because of the omitted fourth layer on top of the q axis. Such layer is normally omitted for ease of manufacturing.

Dealing with the selected $n_{lay} = 3$, this is compatible with the rotor pitch choice and with ease of manufacturing. Although equation (17) would suggest to increase n_{lay} further for minimization of L_{cq}, this would hardly be compatible with the $(n_r = 12 + 4)$ torque ripple golden rule, as more layers would necessarily lead to a shorter rotor pitch.

Regarding with the flow-through inductance L_{fq}, this is computed as:

$$\frac{L_{fq}}{L_{md}} = \frac{4}{\pi}\,\frac{p\,k_c\,g}{R\,x} \sum_{k=1}^{n_{lay}} \Delta f_k^2\, \frac{s_k}{h_{c,k}} \tag{18}$$

where the barriers dimensions hc_k and s_k are defined in Fig. 3. Details on how the formula was derived from the magnetic circuit model of the q axis are in [17] and [18].

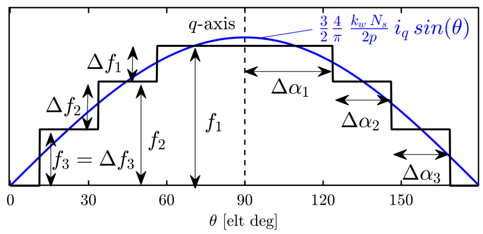

Fig. 4. Sinusoidal stator MMF averaged by the rotor iron carriers.

TABLE I

INPUTS IN COMMON TO ALL CONSIDERED DESIGNS

Number of pole pairs	p	3
Number of slots per pole per phase	q	2
Number of rotor flux barriers	n_{lay}	3
Stator outer radius $[mm]$	R	87.5
Stack length $[mm]$	L	110
Airgap length $[mm]$	g	0.325
Iron flux density, peak $[T]$	B_{Fe}	1.4
Thermal loading factor $[kW/m^2]$	k_j	2.8
Tooth width factor	k_t	0.89
Number of turns in series per phase	N_s	108

The "constant barrier permeance" law (19) is conveniently adopted.

$$\frac{h_{c_k}}{s_k} = \frac{h_{c_1}}{s_1} \tag{19}$$

By substitution of (19) into (18):

$$\frac{L_{fq}}{L_{md}} = \frac{4}{\pi}\,\frac{p\,k_c\,g}{R\,x}\,\frac{\sum_{k=1}^{n_{lay}} s_k}{\sum_{k=1}^{n_{lay}} hc_k}\sum_{k=1}^{n_{lay}} \Delta f_k \tag{20}$$

L_{fq} mainly depends on the sum of the flux barriers lengths $\sum_{k=1}^{n_{lay}} hc_k$ or "total insulation" at the denominator: the thicker the barriers, the lower the flux flowing through the pole and thus the inductance. The summation $\sum_{k=1}^{n_{lay}} s_k$ derives from the barriers positions $\Delta\alpha_k$ and rotor radius, whereas the summation of Δf_k derives from the $\Delta\alpha_k$ angles only.

As said, the total insulation must comply with the iron carries width constraint, i.e. being equal to the available radial space Δr defined in Fig. 3 minus the reference quantity l_y:

$$\sum_{k=1}^{n_{lay}} hc_k = \Delta r - l_y \tag{21}$$

The barriers widths are determined after the total insulation, according to the constant ratio principle (19).[1]

$$hc_k = \sum_{k=1}^{n_{lay}} hc_k \cdot \frac{s_k}{\sum_{k=1}^{n_{lay}} s_k} \tag{22}$$

The validity of the proposed method is independent from the number of rotor barriers.

F. Rotor ribs flux linkage

An additional component of q-axis flux linkage is the one conducted by the rotor ribs, designed for structural integrity of the rotor poles. Such additional q-axis flux path is undesired although inevitable. The related flux linkage is expressed as:

$$\lambda_{rib} = \frac{4}{\pi}\,k_w\,N_s\,w_{rib}\,L \cdot B_{rib} \tag{23}$$

where w_{rib} is the ribs width. In case inner posts or additional ribs are present, their width is added to w_{ribs}, becoming the total ribs width. The parameter B_{rib} is the flux density in the ribs, corresponding to saturated iron. In the paper, $B_{rib} = 2.0\,T$ is used, for the considered iron (M600-50A). The flux linkage component (23) adds to the q-axis flux linkage, to the detriment of torque (4). Its impact is limited by making the ribs as small as possible and thanks to steel saturation. Although this flux component is not proportional to i_q, its impact on torque and power factor is modeled by adding a corresponding q inducance component, $L_{rq} = \lambda_{rib}\,/\,i_q$ to L_{mq}.

G. Slot leakage inductance

The slot leakage inductance L_σ depends on the slot dimensions, defined in Fig. 2. According to [19], the leakage inductance for a single layer distributed winding can be evaluated as:

$$L_\sigma = \frac{2\,\mu_0\,N_s^2\,L}{p\,q}\,p_s \tag{24}$$

where p_s is a permeance factor of the stator slot. With $\beta = c_1/c_2$, the permeance factor is computed as:

$$p_s = \frac{d_0}{c_0} + \frac{d_1}{c_0}\,\frac{ln(\frac{c_1}{c_0})}{\frac{c_1}{c_0}-1} + \frac{d_2}{c_2}\,\frac{\beta^2 - \frac{\beta^4}{4} - ln(\beta) - \frac{3}{4}}{(1-\beta)(1-\beta^2)^2} \tag{25}$$

III. DESIGN PLANE AND MODEL REFINEMENTS

The core of the analytical design process is the x, b parametric design plane [17]. Torque and power factor are reported as a function of x and b and each point of the plane represents a motor design having different rotor diameter (coming from x) and core dimensions (coming from b). Table I reports the set of design inputs that all the machines of the design plane have in common, taken from the SyR machine prototype presented in [21]. The set of inputs contains geometric quantities (R, L, g, p, q, k_t) and the target loading factors $B_{Fe}[T]$ and $k_j[W/m^2]$.

Given the geometry and the number of turns, k_j determines the nominal current i_0 (3), sum of i_d and i_q vector components. The d-axis sizing equation (16) dictates the excitation current i_d, whereas i_q follow accordingly:

$$k_j \overset{eq.(3)}{\rightarrow} i_0, B_{Fe} \overset{eq.(16)}{\rightarrow} i_d, i_q = \sqrt{i_0^2 - i_d^2} \tag{26}$$

The current phase angle γ is implicitly defined by (26) as $i_d = i_0\,cos(\gamma), i_q = i_0\,sin(\gamma)$.

A. Initial Design Plane and FEA Validation

Fig. 5 shows the torque and power factor x, b plane results, using the input data of Table I. The torque contours (5) are plotted in red, the power factor contours (7) in blue. Three

---

[1] The quantity Δr is unknown apriori, because of the implicit definition of $hc_1/2$, as indicated in Fig. 3.

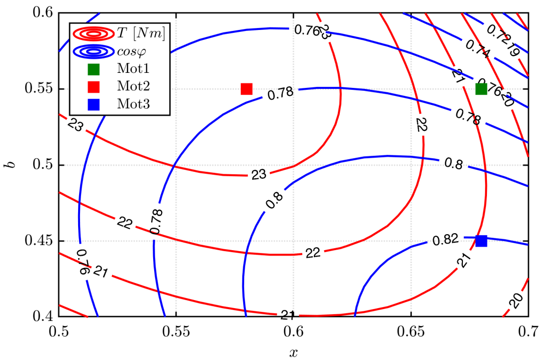

Fig. 5. Parametric design plane obtained with the analytical model: Torque (red contours) and power factor (blue contours) function of x and b

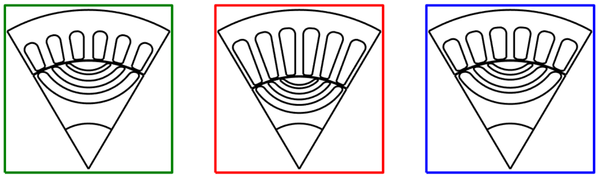

(a) (b) (c)

Fig. 6. Design examples from the xb-plane: Mot1 (a), Mot2 (b) and Mot3(c)

machines are extracted from the plane, represented in Fig. 6. They are:

- **Mot1**: is the prototype motor presented in [21], having $x = 0.68$ and $b = 0.55$
- **Mot2**: with $x = 0.58$ and $b = 0.55$, highlights the effect of x variation.
- **Mot3**: with $x = 0.68$ and $b = 0.45$, highlights the effect of b variation.

The dimensions of the three machines are reported in Table II. Moving from Mot1 to Mot2 in the plane, the x reduction increases the slot area, resulting in higher slot current and ultimately output torque. The $cos\varphi$ does not vary significantly. Dealing with the effect of b, moving from Mot1 to Mot3 produces a design with thinner iron paths, larger stator slots and rotor air barriers. In this case the power factor improves from Mot3 to Mot1, whereas no significant torque variation is expected from Fig. 5.

All the machines of the x, b domain were FEA simulated to build the reference torque and power factor contours, to be compared to the ones coming from the design equations. Fig. 7a and Fig. 7b report the torque and power factor comparisons, respectively. Dashed lines stand for FEA results and solid lines stand for the design equations, called the 'Initial Model'. The model error is evident: the torque of Mot1 is overestimated by the initial model up to 5 Nm (21 Nm against 16 Nm), while the $cos\varphi$ of Mot2 is estimated to be 0.77 instead of 0.73. Furthermore, the contours produced by the equations look different from the FEA ones. The analytical model lacks of accuracy both quantitatively and qualitatively.

TABLE II
MAIN SIZES OF THE THREE DESIGN EXAMPLES

		Mot1	**Mot2**	**Mot3**
x	[-]	0.68	0.58	0.68
b	[-]	0.55	0.55	0.45
$\Delta\alpha$	[°]	11.25 − 7.5 − 7.5		
r	$[mm]$	59.5	50.75	59.5
$h_{c,1}$	$[mm]$	2.38	1.85	2.59
$h_{c,2}$	$[mm]$	4.15	3.17	4.41
$h_{c,3}$	$[mm]$	5.83	4.43	6.32
s_1	$[mm]$	6.32	5.35	6.32
s_2	$[mm]$	11.15	9.48	11.15
s_3	$[mm]$	15.69	13.35	15.69
w_t	$[mm]$	5.08	4.34	4.16
l_y	$[mm]$	11.50	9.81	9.41
l_t	$[mm]$	16.17	26.61	18.26
c_0	$[mm]$	3.13	2.67	3.13
c_1	$[mm]$	5.57	4.77	6.53
c_2	$[mm]$	8.18	9.22	9.47
d_0	$[mm]$	0.60		
d_1	$[mm]$	0.57	0.49	0.79
d_2	$[mm]$	15.00	25.52	16.86

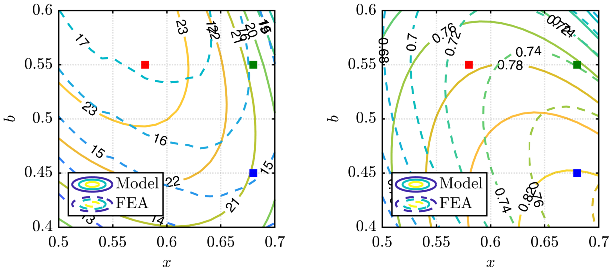

(a) (b)

Fig. 7. Comparison between the initial model estimation (solid lines) and the FEA simulation (dashed lines) of torque (a) and power factor (b) evaluated in the working point defined by the loading factors.

B. Proposed Model Refinements

Two refinements are presented in the following sections, to improve the accuracy of the initial design plane based on (1). Three correction factors are introduced in the refined flux linkage equations (27):

$$\begin{cases}\lambda_d = k_{cross,d}\,(\frac{L_{md}}{k_{sat}} + L_\sigma)\cdot i'_d \\ \lambda_q = k_{cross,q}\,(L_{mq} + L_\sigma)\cdot i'_q\end{cases} \qquad (27)$$

The factor k_{sat} accounts for the reduction of the magnetizing inductance L_{md} due to direct saturation of the d axis. The two factors $k_{cross,d}$ and $k_{cross,q}$ correct the cross-saturation effect and all residual errors, using the fast FEA approach called FEAfix. The apostrophes on the current components i'_d, i'_q indicate that upon including saturation into the equations, also the operating point varies from previously determined i_d, i_q. Since the peak flux density is imposed, the magnetizing current augments to $i'_d = k_{sat}\, i_d > i_d$ when accounting for saturation. By consequence, the q current component reduces as $i'_q < i_q$, according to (26). If i'_d is higher than i_0, the

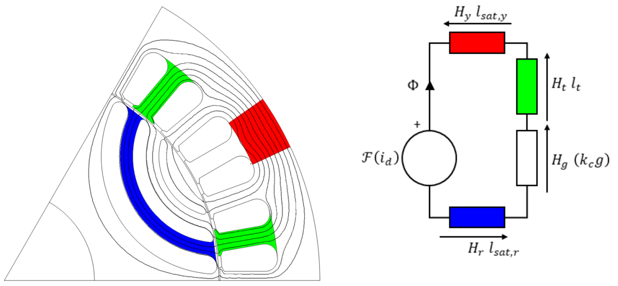

(a) (b)

Fig. 8. Iron section added to the d-axis model for the saturation factor computation (a) and equivalent circuit (b)

design is not feasible with the selected loading factors and it is reported as an error on the design plane.

C. Saturation factor k_{sat}

The initial d-axis model neglected the MMF drop into the iron core, leading to L_{md} overestimate and i_d underestimate. The proposed refinement modifies the $d-$MMF equation (15) using the simple magnetic circuit model of Fig. 8. A single flux tube, representative of the most loaded parts of the machine core along the d-axis, is considered. The regions of such flux tube are:

- Two stator teeth (iron length equal to $2\, l_t$), shown in green
- One section of the stator yoke between two teeth (iron length equal to $l_{sat,y} = \frac{\pi}{3pq}(R - \frac{l_y}{2})$), highlighted in red
- One rotor flux carrier (iron length equal to $l_{sat,r}$), colored in blue

The magnetic circuit model is reported in Fig. 8b, using the same color code of sub-figure (a). The Ampere's law applied the considered flux tube is:

$$\frac{3}{\pi}\,\frac{k_w\, N_s}{p}\, i_d = H_g \cdot k_c\, g + H_t \cdot l_t + H_y \cdot l_{sat,y} + H_r \cdot l_{sat,r} \quad (28)$$

Where $H_g \cdot k_c\, g = \frac{B_{Fe} b}{\mu_0} k_c\, g$ is the airgap MMF drop, same as in (15). The other terms on the right hand side account for the non-ideal iron. The magnetic fields $H_t = H\left(\frac{B_{Fe}}{k_t}\right)$ and $H_y = H_r = H\,(B_{Fe})$ in the considered iron sections are obtained from the $B - H$ curve of the steel lamination, imposing the reference flux densities. With the airgap term in evidence, equation (28) is rewritten in the form of (15):

$$\frac{3}{\pi}\,\frac{k_w\, N_s}{p}\, i_d = \left(\frac{k_c\, g}{\mu_0}\, B_{Fe}\, b\right) \cdot k_{sat} \quad (29)$$

Where the saturation factor k_{sat} is:

$$k_{sat} = 1 + \frac{H_t\, l_t + H_y\, (l_{sat,y} + l_{sat,r})}{H_g\, (k_c\, g)} > 1 \quad (30)$$

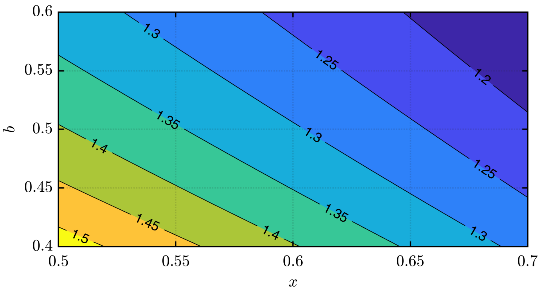

Fig. 9. Saturation factor values for the case study in Table I

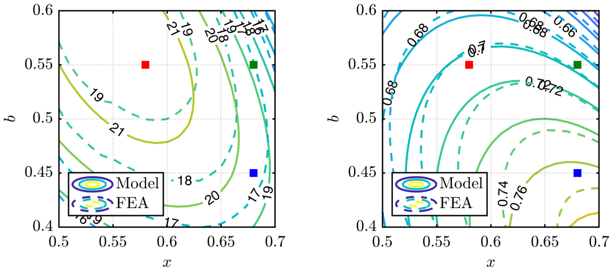

(a) (b)

Fig. 10. Comparison between the analytical model with saturation factor (solid lines) and the FEA simulations (dashed lines) on torque (a) and power factor (b)

Substituting explicit geometric quantities (referred to half pole, for symmetry), the saturation factor becomes:

$$k_{sat} = 1 + \mu_0\, \frac{H_t\, l_t + H_y\, \left[\left(R - \frac{l_y}{2}\right)\frac{\pi}{6\,p\,q} + \frac{s_{n_{lay}} + s_{n_{lay}-1}}{2}\right]}{k_c\, g\, B_{Fe}\, b} \quad (31)$$

As the flux density is imposed in all the sections of the flux tube, k_{sat} (31) is explicitly evaluated without need of iteration. By comparison of (15) and (29), the magnetizing current varies from i_d to $i'_d = k_{sat}\, i_d$.

D. FEA validation of k_{sat}

Fig. 9 shows k_{sat} as a function of x, b, for the considered case study. The saturation effect increases inversely to both x and b. This is because the tooth length l_t is inversely proportional to both x and b, and so is the corresponding MMF drop. By comparing Fig. 7 and Fig. 9 it can be noticed that the k_{sat} value is higher where the FEA versus initial model discrepancy is higher, while where the discrepancy is lower is where k_{sat} is closer to one.

The use of k_{sat} on top of the initial model allows to improve the matching between the design equations contours and the FEA results. Fig. 10 reports the results after this upgrade, with the FEAfix correction factors not yet applied: both torque (Fig. 10a) and power factor (Fig. 10b) contours show evident improvements.

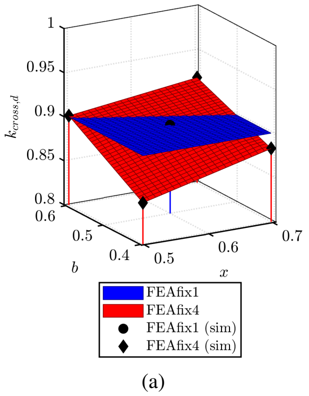

(a) (b)

Fig. 11. Cross-saturation factors $k_{cross,d}$ (a) and $k_{cross,q}$ (b) over the x, b plane. Blue: using 1 FEA simulation (FEAfix1 - black dot). Red: using4 FEA simulations (FEAfix4 - black diamonds).

E. Fast FEA fix of residual errors (FEAfix)

Cross saturation modifies each flux linkage component (e.g. d) in presence of current on the other axis (e.g. q). Computing the effect of cross-saturation with a purely analytical approach is quite complicated [22] and not accurate enough to the purpose of machine design.

The proposed solution corrects the analytical model using the coefficients $k_{cross,d}$ and $k_{cross,q}$ defined in (27). Selected designs in specific points of the x, b plane are FEA simulated, with limited computational time. The simplest FEAfix scheme is called here FEAfix1 and FEA evaluates a single machine of the whole x, b plane, the one in the center, indicated with a black circle in the following. In turn, upon FEA evaluating the d, q flux linkages of one design of the plane, the correction coefficients are evaluated for that machine according to (32-33), and applied to all the designs of the plane:

$$k_{cross,d} = \frac{\lambda_{d,FEAfix1}}{\left(\frac{L_{md}}{k_{sat}} + L_\sigma\right) i'_d} \tag{32}$$

$$k_{cross,q} = \frac{\lambda_{q,FEAfix1}}{\left(L_{mq} + L_\sigma\right) i'_q} \tag{33}$$

The subscript *FEAfix1* indicates the FEA results for the machine in the center of the plane. Fig. 11 shows the correction factors in the x, b plane for the considered case study. The black circular dot in the center of the plane indicates the position of the FEAfix1 evaluated design. The blue surfaces are the FEAfix1 d and q coefficients, constant in the x, b domain.

The further accurate FEAfix4 method consists of FEA evaluating the four machines at the corners of the design domain. The correction factors obtained for the four simulated cases are extended to the full x, b plane using bi-linear interpolation. The results of FEAfix4 are represented by the red surfaces of Fig. 11. The four FEA-evaluated points are tagged with black diamonds. Expectedly, the correction factors are consistently lower than one, confirming that the pure analytical model tends to overestimate the machine flux linkages.

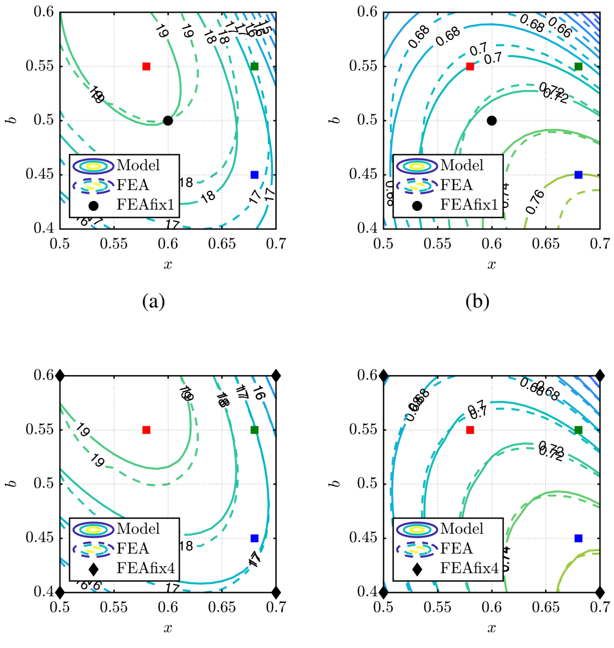

(a) (b)

(c) (d)

Fig. 12. Comparison between the performance figures estimated with the FEAfix models and the FEA validation. Torque (a) and power factor (b) of FEAfix1 model and torque (c) and power factor (d) of FEAfix4 model.

F. FEA validation of FEAfix1 and FEAfix4

The torque and power factor curves obtained with refined model (27) are compared against the complete FEA results (as done for the other models). Figs. 12-a -b refer to FEAfix1 and Figs. 12-c -d refer to FEAfix4. With both k_{sat} and FEAfix corrections, the model and FEA contours are practically superimposed. The maximum accuracy is reached, expectedly, in the regions around the FEAfix simulation points, tagged in black in the figures.

IV. COMPARATIVE ANALYSIS

This section compares all proposed modelling steps in terms of accuracy and computational time, using FEA results as the common term of comparison. The simulations are performed for each geometry at the working point computed from the design plane. The four considered models are:

- **Initial**, marked in red in the next figures. It is the one with ideal iron and $k_{sat} = k_{cross,d} = k_{crossq} = 1$.
- **Saturated**, marked in green. The factor $k_{sat} > 1$ is considered, whereas $k_{cross,d} = 1$, $k_{cross,q} = 1$.
- **FEAfix1**, marked in blue. Here $k_{sat} > 1$ plus FEAfix1-calculated $k_{cross,d} < 1$, $k_{cross,q} < 1$ are used.
- **FEAfix4**, marked in orange. Here $k_{sat} > 1$ plus FEAfix4-calculated $k_{cross,d} < 1$, $k_{cross,q} < 1$ are used.

First, the machine examples Mot1, Mot2, Mot3 are used as term for comparison. Then precision versus computational time is considered. Finally, the sensitivity towards the input

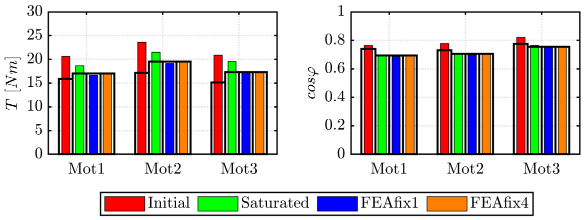

Fig. 13. Comparison between the analytical models and FEA results for the three benchmark machines.

TABLE III
COMPARISON BETWEEN ANALYTICAL MODELS AND FEA FOR THE THREE BENCHMARK MACHINES

		T $[Nm]$			$cos\varphi$		
		Mot1	Mot2	Mot3	Mot1	Mot2	Mot3
Initial	Model	20.6	23.6	20.9	0.764	0.777	0.821
	FEA	15.9	17.2	15.1	0.739	0.730	0.775
Saturated	Model	18.7	21.5	19.5	0.692	0.706	0.765
	FEA	17.0	19.5	17.3	0.694	0.706	0.755
FEAfix1	Model	16.6	19.2	17.4	0.688	0.699	0.759
	FEA	17.0	19.5	17.3	0.694	0.706	0.755
FEAfix4	Model	17.1	19.4	17.2	0.697	0.707	0.756
	FEA	17.0	19.5	17.3	0.694	0.706	0.755

loading factors B_{Fe} and k_j and the ribs flux density B_{rib} is evaluated.

A. Comparison of Designs Mot1, Mot2 and Mot3

The three benchmark machines introduced in section III are considered. Fig. 13-a and -b show the torque and power factor figures of the three benchmark machines, estimated by the models (colored bars), versus FEA results (transparent bars with black contour). The FEA reference of the red initial model is different because of the different operating point (i_d in place of i'_d). The initial model (red bars) overestimates torque by 4-6 Nm (30% circa), while the power factor is slightly overestimated (5% circa). The use of the saturation factor (green bars) strongly improves the torque accuracy, thanks to the improvement on the L_{md} estimation. Also the power factor accuracy improves, for all motors. The FEAfix1 (blue) and FEAfix4 (orange) estimates go very close to zero error. The values of Fig. 13 are reported in Table III to highlight the high precision obtained from FEAfix models.

B. Trade off between Accuracy and Computational Time

The trade-off between the computational time and the model precision is summarized in Fig. 14 and Table IV. The computational time needed to evaluate each model is reported on the x axis, while the average torque and power factor errors among the design plane are reported on the y axis. The brute force approach (651 designs FEA evaluated over the entire x, b plane) is included on the plot for a sake of comparison. A desktop computer with Intel i7-4770, 3.2GHz processor and 16 GB RAM was used.

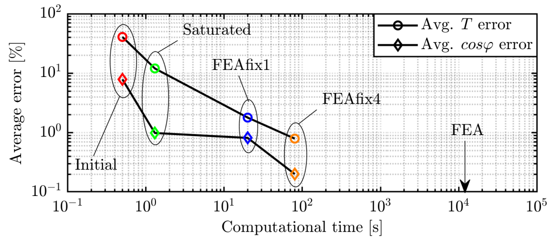

Fig. 14. Time versus accuracy tradeoff of the four proposed models: torque and power factor error averaged on the design plane versus computational time.

TABLE IV
TRADEOFF BETWEEN COMPUTATIONAL TIME AND PRECISION

	Comp. time $[s]$	Avg. T error [%]	Avg. $cos\varphi$ error [%]
Initial	0.5	41	7.9
Saturated	1.3	12	1.0
FEAfix1	20	1.8	0.8
FEAfix4	80	0.8	0.2
FEA	13020	–	–

The analysis reveals that, expectedly, the four approaches increase the accuracy at the expense of progressively increasing computational time: to increase the model precision, a higher computational time is required, and vice versa. The saturation factor increases the computational time from 0.5 to 1.3 seconds (2.6 more, and 10.000 less than brute force), cutting the average torque error from about 40% to 12% and the power factor error from 8% to 1%. The FEAfix correction further cuts the errors at the cost of approximatively 20 s more computation per each FEAfix simulation (20 s extra for FEAfix1, 80 s extra for FEAfix4). This means 650 and 325 times less than the brute force case, respectively.

In turn, the most convenient improvement comes from k_{sat}, which cuts the error significantly with seamless extra computation. FEAfix1 is retained more convenient than FEAfix4: it requires only one fourth of the computational effort to reach almost the same accuracy. In any case, all proposed solutions are retained very convenient, if compared to the time required to FEA evaluate the entire design domain. The use of an optimization algorithm might, in principle, reduce the brute-force computational time, but vanishes the beauty and insight of having all the x, b plane available to the designer.

C. Sensitivity Against B_{Fe} and k_j

The proposed methods are validated against the key design inputs B_{Fe} and k_j. Six cases are studied, corresponding to two values of k_j ($2.8\,kW/m^2$ and $5.0\,kW/m^2$) and three values of iron flux density ($B_{Fe} = 1.3\,T$, $1.4\,T$ and $1.5\,T$). The results are presented for Mot1 only, for the sake of simplicity, but the insights hold for the whole design plane, as verified off-line by the authors.

Fig. 15 shows the error on torque and power factor prediction for the six mentioned combinations. As before, the colored bars represent the results from the different models, while the black-contoured transparent bars refer to the FEA results. For the sake of clarity, the initial model uses the same operating point i'_d, i'_q of the other models. The results are consistent to the ones reported in the previous section, also in presence of k_j and B_{Fe} variation. The FEAfix results are the more stable against parameter variation: the precision is practically

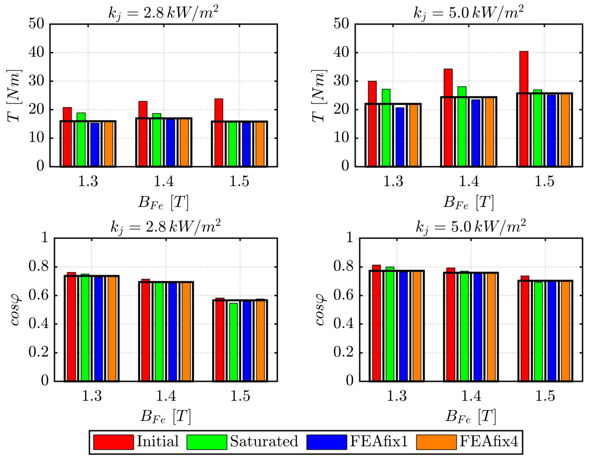

Fig. 15. Sensitivity of the performance errors (T and $cos\varphi$) against B_{Fe} and k_j for the four considered models, compared with FEA.

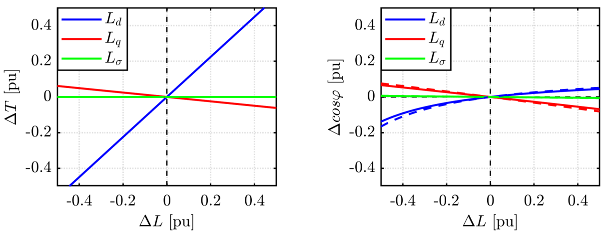

(a) (b)

Fig. 16. Effects of the inductance variation on the torque estimation (a) and power factor estimation (b). Torque plot valid for each value of γ, power factor shown for $\gamma = 45°$ (solid lines) and $\gamma = 60°$ (dashed lines).

constant for all the considered loading factors combinations. The saturated model is less stable than FEAfix, but much more robust than the initial model. The general conclusion is:

- power factor is better estimated than torque;
- The saturation factor has substantial effect on torque;
- FEAfix leads to approximately zero error.

D. Sensitivity to L_d, L_q, L_s estimates

The effect of the errors in the inductances estimation is investigated, for deeper understanding of the proposed improvements. Fig 16a reports the torque error caused by errors on L_d (blue curve), L_q (red curve) and L_σ (green curve) estimates. Torque estimate is robust against L_q error: +50% on L_q causes a torque deviation of -5.5%. Conversely, the correlation between L_d and torque errors is about one to one. As expected from the torque equation (5), this is insensitive to L_σ.

Fig. 16b repeats the sensitivity analysis for the power factor. As already noticed, power factor is less prone to error than torque, towards all the inductances. The leakage inductance has low impact: -50% on L_σ results in a $cos\varphi$ error of less than 1%. The power factor error is also function of the current angle: for high values of γ, the relative errors slightly increase (dashed lines of Fig. 16b).

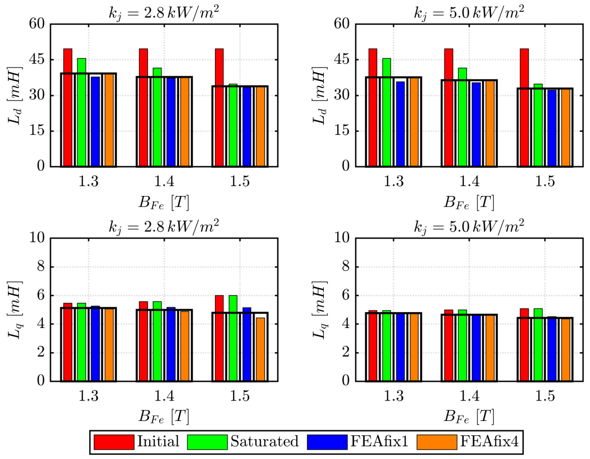

Fig. 17. Sensitivity of the dq inductances errors against B_{Fe} and k_j for the four considered models, compared with FEA.

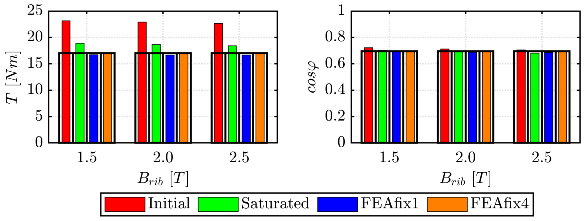

Fig. 18. Sensitivity of torque and PF estimates against B_{rib} (Mot1).

Finally, the inductances L_d and L_q are computed and compared with FEA for all the B_{Fe}, k_j scenarios. The results are reported in Fig. 17. The study confirms that the saturation factor acts on the large error of L_d, and it is effective especially for higher values of B_{Fe}. Dealing with L_q, this is not affected by k_{sat}. According to the analysis on torque and power factor equation, the improvement in L_d estimation reflects in the better torque estimate.

E. Sensitivity Against B_{rib}

One of the critical parameters in the estimation of the machine performance is the ribs flux density B_{rib}. This value is set at the beginning of the procedure and it is kept constant. Moreover, the final value could be different. To state the sensitivity against this input, three cases are studied, with B_{rib} equal to $1.5\,T$, $2\,T$ and $2.5\,T$. Only Mot1, with benchmark case $k_j = 2.8\,kW/m^2$ and $B_{Fe} = 1.4\,T$ is considered for a space limit, but the conclusion of the analysis are verified off-line by the authors on the other scenarios and designs.

Torque and power factor are poorly affected by B_{rib} change and FEAfix models are almost insensitive to B_{rib}, as shown in Fig. 18. The low effect comes from the inductance errors: B_{rib} affect only L_q and not L_d. Indeed, the effect of L_q errors reflect in a limited misestimate of T and $cos\varphi$, according to Fig. 16.

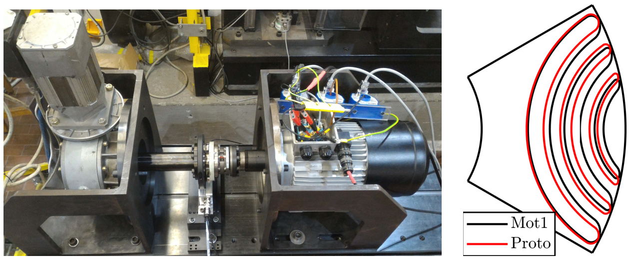

(a) (b)

Fig. 19. Test rig for the experimental validation (a) and rotor comparison between Mot1 and the prototype (b).

V. EXPERIMENTAL VALIDATION

The proposed models are validated with experimental tests on an existing prototype. The machine, presented in [21], was designed using Multi-Objective Optimization Algorithm, targeting an improvement of torque and a reduction of torque ripple. It has the same stator of Mot1 and slightly different rotor geometry, as reported in Fig. 19b. The differences between Mot1 and the actual prototype are investigated in [21]. To validate the models, the flux maps in the $i_d - i_q$ plane are computed with FEA and experimentally measured. Then, the torque and power factor corresponding to the working point (i'_d, i'_q) are extracted and compared with the model results. For the simulations, the routines included in SyR-e [14] are adopted. They use FEMM [15] as FEA software. The identification results are the dq flux linkages and torque function of the dq currents. Power factor is computed using (6). Regarding the experiments, the adopted identification methodology is described in [23]. The results are in the same form of FEA simulations: flux linkages and torque maps function of the dq currents.

Fig. 19a shows a picture of the prototype (on the right) on the test bed used for the experimental validation. The prototype is supplied with a custom inverter, controlled with a dSPACE DS1103 fast control prototyping board. Currents, voltages and torque measurements are collected with an HBM GEN3i data recorder.

Fig. 20 compares torque (a) and power factor (b) estimates from the four design models of the actual geometry, compared to FEA and experiments. The FEA model and experimental measures have a discrepancy of about 3% on torque and 9% on power factor. This derives from the manufacturing process tolerances. According to the previous analysis, the initial model has the highest error on torque (+38%) and power factor (+8.5%). The other models (saturated, FEAfix1 and FEAfix4) are close to FEA results.

VI. CONCLUSION

In this paper a new approach to SyR machine design was proposed and validated. The proposed procedure is based on an analytical model, that is improved in two steps. Each proposed improvement is compared with the others in terms of accuracy, computational time and robustness against input variation. The first improvement deals with the real B-H curve and gives a drastic reduction of torque and power factor estimation errors (from 41% to 12% and from 8% to 1% respectively). Computational time is slightly higher, but no iterations to account for the non-linear B-H curve are adopted. The second improvement, called FEAfix, further improve the accuracy by simulating one (FEAfix1) or four (FEAfix4) relevant machines (and not necessarily the "best" machine). The computational time is increased and the model are robust against parameter variation. Moreover, the computational effort is negligible compared to the brute-force full-FEA approach, while the precision and robustness are almost the same. Bottomline, FEAfix models presents FEA-like accuracy and robustness, with the computational time and the insight on the design proper of analytical models, showing to be promising shortcut for present and future designers.

Experimental measurements on an existing prototype further support the FEA validation of the proposed models. Finally, the FEAfix methodology is now part of the SyR-e motor design project.

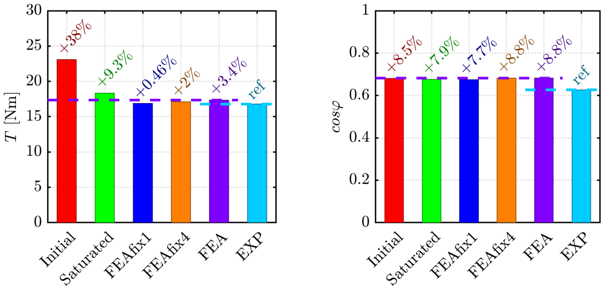

(a) (b)

Fig. 20. Validation of the proposed model against FEA and experimental results on the tested prototype.

REFERENCES

[1] A. T. de Almeida, F. J. T. E. Ferreira, and G. Baoming, "Beyond induction motors—technology trends to move up efficiency," *IEEE Transactions on Industry Applications*, vol. 50, no. 3, pp. 2103–2114, May 2014.

[2] M. Ferrari, N. Bianchi, A. Doria, and E. Fornasiero, "Design of synchronous reluctance motor for hybrid electric vehicles," *IEEE Transactions on Industry Applications*, vol. 51, no. 4, pp. 3030–3040, July 2015.

[3] K. Grace, S. Galioto, K. Bodla, and A. M. El-Refaie, "Design and testing of a carbon-fiber-wrapped synchronous reluctance traction motor," *IEEE Transactions on Industry Applications*, vol. 54, no. 5, pp. 4207–4217, Sep. 2018.

[4] H. Mahmoud, N. Bianchi, G. Bacco, and N. Chiodetto, "Nonlinear analytical computation of the magnetic field in reluctance synchronous machines," *IEEE Transactions on Industry Applications*, vol. 53, no. 6, pp. 5373–5382, Nov 2017.

[5] I. Boldea, *Reluctance synchronous machines and drives.* Oxford University Press, 1996.

[6] H. Shao, S. Li, and T. G. Habetler, "Analytical calculation of the air-gap flux density and magnetizing inductance of synchronous reluctance machines," in *2018 IEEE Energy Conversion Congress and Exposition (ECCE)*, Sep. 2018, pp. 5408–5413.

[7] S. Taghavi and P. Pillay, "A sizing methodology of the synchronous reluctance motor for traction applications," *IEEE Journal of Emerging and Selected Topics in Power Electronics*, vol. 2, no. 2, pp. 329–340, June 2014.

[8] R. Moghaddam and F. Gyllensten, "Novel high-performance synrm design method: An easy approach for a complicated rotor topology," *IEEE Transactions on Industrial Electronics*, vol. 61, no. 9, pp. 5058–5065, Sep. 2014.

[9] M. D. Nardo, G. L. Calzo, M. Galea, and C. Gerada, "Design optimization of a high-speed synchronous reluctance machine," *IEEE Transactions on Industry Applications*, vol. 54, no. 1, pp. 233–243, Jan 2018.

[10] E. Howard, M. J. Kamper, and S. Gerber, "Asymmetric flux barrier and skew design optimization of reluctance synchronous machines," *IEEE Transactions on Industry Applications*, vol. 51, no. 5, pp. 3751–3760, Sep. 2015.

[11] Y. Wang, D. M. Ionel, M. Jiang, and S. Stretz, "Large scale optimization of electronically controlled synchronous reluctance machines using ce-fea and differential evolution," in *2015 IEEE International Electric Machines Drives Conference (IEMDC)*, May 2015, pp. 1702–1708.

[12] M. H. Mohammadi, T. Rahman, R. Silva, M. Li, and D. A. Lowther, "A computationally efficient algorithm for rotor design optimization of synchronous reluctance machines," *IEEE Transactions on Magnetics*, vol. 52, no. 3, pp. 1–4, March 2016.

[13] S. Ferrari and G. Pellegrino, "Fea-augmented design equations for synchronous reluctance machines," in *2018 IEEE Energy Conversion Congress and Exposition (ECCE)*, Sep. 2018, pp. 5395–5402.

[14] F. Cupertino, G. Pellegrino, and et al., "Syr-e: Synchronous reluctance (machines) - evolution," accessed 24-January-2019. [Online]. Available: https://sourceforge.net/projects/syr-e/

[15] D. Meeker, "Femm: Finite element method magnetics." [Online]. Available: http://www.femm.info/

[16] D. A. Staton, T. J. E. Miller, and S. E. Wood, "Maximising the saliency ratio of the synchronous reluctance motor," *IEE Proceedings B - Electric Power Applications*, vol. 140, no. 4, pp. 249–259, July 1993.

[17] I. Boldea, T. Fukao, T. A. Lipo, L. Malesani, T. J. E. Miller, and A. Vagati, "Synchronous reluctance motors and drives: a new alternative," in *Tutorial Course at the IEEE-IAS Annual Meeting*, 1994.

[18] A. Vagati, G. Franceschini, I. Marongiu, and G. P. Troglia, "Design criteria of high performance synchronous reluctance motors," in *Conference Record of the 1992 IEEE Industry Applications Society Annual Meeting*, Oct 1992, pp. 66–73 vol.1.

[19] T. A. Lipo, *Introduction to AC machine design*. John Wiley & Sons, 2017.

[20] A. Vagati, M. Pastorelli, G. Francheschini, and S. C. Petrache, "Design of low-torque-ripple synchronous reluctance motors," *IEEE Transactions on Industry Applications*, vol. 34, no. 4, pp. 758–765, July 1998.

[21] S. Ferrari, G. Pellegrino, M. Davoli, and C. Bianchini, "Reduction of torque ripple in synchronous reluctance machines through flux barrier shift," in *2018 XIII International Conference on Electrical Machines (ICEM)*, Sep. 2018, pp. 2290–2296.

[22] S. Guha and N. C. Kar, "Saturation modeling and stability analysis of synchronous reluctance generator," *IEEE Transactions on Energy Conversion*, vol. 23, no. 3, pp. 814–823, Sep. 2008.

[23] E. Armando, P. Guglielmi, G. Pellegrino, and R. Bojoi, "Flux linkage maps identification of synchronous ac motors under controlled thermal conditions," in *2017 IEEE International Electric Machines and Drives Conference (IEMDC)*, May 2017, pp. 1–8.